Bull. Chem. Soc. Ethiop. **2023**, 37(2), 427-447.
DOI: https://dx.doi.org/10.4314/bcse.v37i2.13

ISSN 1011-3924
Printed in Ethiopia
Online ISSN 1726-801X

NOVEL SERIES OF THIAZOLE-BASED COMPLXES; CHARACTERIZATION, STRUCTURAL OPTIMIZATION, IN-VITRO AND IN-SILICO ASSESSMENTS AGAINST COVID-19 VIRUS COMPARED TO PALXLOVID DRUG

Riman K. Alnefaie[1], Khlood Abou-Melha[2] and Nashwa El-Metwaly[1,3*]

[1]Department of Chemistry, Faculty of Science, King Khalid University, Abha, Saudi Arabia
[2]Department of Chemistry, Faculty of Applied Science, Umm Al Qura University, Makkah, Saudi Arabia

(Received October 4, 2022; Revised November 16, 2022; Accepted November 18, 2022)

ABSTRACT. New thiazole-based complexes were prepared and suggested to be 1:1 metal to ligand ratio. This formula was built depending on different analyses. Various spectroscopic tools were used to confirm the mode of bonding for the ligand towards the metal ions. The ligand behaved as a neutral bidentate mode towards Cu(II), Co(II) and Ni(II) ions. The DFT method was applied to confirm the nucleophilicity of O(13) and N(2) atoms which qualified for excellent coordination. The new compounds were *in-silico* tested against 6lu7 and 6lzg as the main protease complex of COVID-19 and the receptor of coronavirus spike, respectively. This is according to the recent use of a thiazole-based compound (ritonavir) in treatment of COVID-19. This study was extended to handle the paxlovid antiviral (nirmatrelvir and ritonavir) in comparing to new compounds. The ritonavir drug as well as the Co(II) complex appeared as promising inhibitors. To deepen the study, we tested the cytotoxicity of the complexes and interestingly, the Co(II) complex showed a vital inhibition for liver and prostate cancers which exceeds 5-fluorouracil drug.

KEY WORDS: New complexes, Spectral studies, Molecular modelling, In-silico methods towards COVID-19

INTRODUCTION

Corona virus is receiving attention from the whole world, and many researchers are placing special importance in their research to help overcome the risk of infection. In recent years, promising medicines for the corona family have been discovered and are presently being examined for COVID-19, even though the studies have not been finished, and all drugs are already being examined [1]. Because of the exceptionally high ratio of viral enzyme mistakes that are accountable for their genetic reproduction, RNA viruses are exceptionally adaptable to changes [2]. While several elements, such as genetic differences in viruses and some external conditions, have a role in the development of diseases, these viruses are accountable for several new and re-emerging diseases [3]. This virus was shown to be vulnerable to high temperatures (heat) and to be inhibited by a modest number of lipid solvents [4]. Umifenovir is a wider antiviral agent that has been approved as an anti-influenza medication (arbidol). The Academy of Chemical and Pharmaceutical Science in Russia has been developing an antiviral medication for the treating of influenza A and B for about 25 years. It has been registered since 2004 for use as a SARS virus treatment [5]. In 2014, Japan produced favipiravir (avigan), as a medication for novel or persistent influenza viruses. Purine nucleosides are substituted for ribosyl binding and intracellular phosphorylation to stimulate and assemble them into viral RNA. RNA-dependent RNA polymerase will then destroy viruses, preventing RNA strain growth and virus propagation [6]. Idoxuridine is a herpes antiviral medication. It's a nucleoside derivative with a changed deoxyuridine structure that's similar enough to be absorbed into viral DNA replication, but the iodine atom inserted to the uracil part prevents primary conjugation. Because of its cytotoxicity, it is only applied topically. Idoxuridine was initially used as an antiviral drug in 1962 [7].

*Corresponding author. E-mail: n_elmetwaly00@yahoo.com ; nmmohamed@uqu.edu.sa

Heterocyclic compounds are important structures in medication discovery and design, because of their biological characteristics [8]. Thiazole is a powerful nucleus due to its extensive therapeutic applications. Thiazoles and their bivalent metal ion complexes were shown to have a variety of biological activities, including antioxidants, analgesics, anti-hypertensive, anti-cancer, anti-allergic, anti-malarial, anti-inflammatory, anti-psychotic, antibacterial and anti-fungicide properties [9]. Ni(II), Co(II) and Cu(II) were prepared from 2-(4-sulfadiazine)hydrazono dimedone and then investigated after that their binding efficiency with DNA was verified [10]. In a promising investigation of H1V-antiviral drugs, the performance of pyrazole-based anti-influenza agents was explored [11]. In addition, pyrazole derivatives contained inhibitors of herpes simplex viruses (HSV-1) and HIV-1 transcriptase [12]. Molecular docking that employing structurally dependent technique [13] was recommended for the synthesis of new thiazole functionalized as a prospective HCV inhibitor. Following that, the use of tri-substituted thiazoles as anti-flavivirus targeted drugs [14] was explored. Thiazole compounds have antiviral activity against a number of common viral infections. After characterization, distorted square planer geometry was suggested for two Cu(II)- benzimidazole complexes through the legation of NN donors. The antibacterial activity of these reported complexes was investigated versus *E. coli* and *S. aureus* [15]. The vital role of Co(II) and Ni(II) ions inside the cells cannot ignored, Co(II) is the component of vitamin B12 and is the co-enzyme of methylmalonyl mutase and methionine. However, nickel, in particular, is important for human health because it is required by microorganisms that live in distinct development niches throughout the body [16]. These findings opens the door for scientists' efforts, to serve their knowledge on searching on effective therapy for various diseases as COVID-19 or cancer cells, that we already done in this study. Starting from the biological history of thiazole-based compounds, we chose to develop a novel thiazole derivative to prepare its Co(II), Ni(II), and Cu(II) complexes. Then, all available analyses were used to characterize the new compounds. Furthermore, molecular modeling was used to emphasize the structures that were indicated. We're also interested in performing *in-silico* test for the new compounds to evaluate their effectiveness towards the current corona virus (COVID-19). This *in-silico* investigation was reinforced by comparisons with Paxlovid drug that recently used to treat COVID-19. This drug contains two antivirals as nirmatrelvir and ritonavir that is from thiazole family. Regarding the similarity of thiazole-based moiety with ritonavir drug, we intend this comparison hoping to get promising antiviral among our new compounds. Additionally, the cytotoxicity of these complexes was investigated *in-vitro* against three carcinoma cell lines to deep the biological application.

EXPERIMENTAL

Chemicals and reagents

The reagents and chemicals that utilized in this study to prepare the thiazole-based ligand or its complexes were utilized from Sigma and Aldrich or Merck. All these chemicals are extra-pure and having the BDH nature. Further, the ethanol (EtOH), dimethylformamide (DMF) and dimethyl sulfoxide (DMSO) as the solvents used for synthesis or analysis were taken from Sigma and Aldrich and have a spectroscopic purity and consequently used without purification.

*Synthesis of 2-amino-5-(4-ethoxycarbonyl-phenylazo)thiazole (**3**)*

A well-stirred suspension of ethyl 4-aminobenzoate **(2)** (1.65 g, 0.01 mol) in concentrated HCl (3 mL) and H_2O (5 mL) was cooled in ice bath and diazotized with a solution of $NaNO_2$ (0.7 g, 0.01 mol) in 10 mL water. The freshly prepared diazonium solution was slowly added to a well stirred solution of 2-aminothiazole **(1)** (1 g, 0.01 mol) and sodium acetate (3 g) in ethyl alcohol (30 mL). The reaction mixture was stirred at 0-5 °C for 2 h. The product was filtered, dried well and recrystallized from ethyl alcohol. Reddish brown crystals, yield = 90%, m.p. 210-212 °C. IR

(KBr): ν_{max}/cm^{-1}: 3341, 3337 (NH_2), 1693 (C=O), 1650 (C=N). ^1H NMR (DMSO-d_6): δ_{ppm} 1.32 (t, J = 7.0 Hz, 3H, CH_3), 4.31 (q, J = 7.1 Hz, 2H, CH_2), 7.70 (d, J = 8.40 Hz, 2H, Ar-H,), 8.01 (d, J = 8.40 Hz, 2H, Ar-H), 8.15 (s, 1H, thiazole-H_4), 8.61 (s, 2H, exchangeable by D_2O, NH_2). Analysis for $C_{12}H_{12}N_4O_2S$ (276.07): calcd: C, 52.16; H, 4.38; N, 20.28%. Found: C, 52.00; H, 4.41; N, 20.20%.

*Synthesis of 2-chloroacetamido-5-(4-ethoxycarbonyl-phenylazo)-thiazole (**4**)(CET)*

To a suspension of 2-aminothiazole derivative **3** (1.38 g, 0.005 mol) and anhydrous K_2CO_3 (0.7 g, 0.005 mol) in dry dimethylformamide (20 mL), chloroacetyl chloride (0.8 mL, 0.01 mol) was added. The mixture was stirred at 25-30 ºC for 4 h and then poured onto ice cold water. The resulting precipitate was filtered, dried and recrystallized from ethyl alcohol. Orange crystals, yield = 59%, m.p. 220-222 ºC. IR (KBr): ν_{max}/cm^{-1}: 3160 (NH), 1723, 1688 (C=O). ^1H NMR (DMSO-d_6): δ_{ppm} 1.34 (t, J = 7.0 Hz, 3H, CH_3), 4.35 (q, J = 7.1 Hz, 2H, CH_2), 4.48 (s, 2H, CH_2), 7.84 (d, J = 8.40 Hz, 2H, Ar-H), 8.08 (d, J = 8.40 Hz, 2H, Ar-H), 8.53 (s, 1H, thiazole-H_4), 12.99 (s, 1H, exchangeable by D_2O, CONH). Analysis for $C_{14}H_{13}ClN_4O_3S$ (352.04): calcd: C, 47.66; H, 3.71; N, 15.88%. Found: C, 47.85; H, 3.77; N, 15.79%.

Synthesis of metal ion complexes

Equi-molar fraction (5mmol) from each of $CoCl_2.6H_2O$ (1.189 g), $NiCl_2.6H_2O$ (1.188 g) or $CuCl_2.2H_2O$ (0.852 g) salt was dissolved in EtOH solvent and then mixed with thiazole derivative (CET) (1.760 g) to generate the new complexes. The reaction mixtures were kept under reflux (at 75 ºC) for a long time without remarkable changes. As known, the used salts have relatively acidic nature in reaction mixture due to presence of chloride anion, so the addition of 1g NaOAc (dissolved in few drops of dist. water) could elevate the reaction pH slightly (~5). The colors of reaction mixtures are changed suddenly, which considered the preliminary evidence for complexation. Then the reaction mixtures were maintained under reflux overnight for precipitation. The slight basicity of acetate anion helps the reaction to complete and complex precipitation. Filtered colored precipitates which were removed and then washed with EtOH. Under $CaCl_2$, the specimens were put in closed desiccators for drying. Table 1 shows the results of some analyses, for studying.

Techniques used

The majority of the instruments used for analysis are found in Mansoura and Cairo Universities. However the measuring conditions were mostly included in the discussion section. While, the ^1H NMR spectra of the organic compounds were obtained using a Bruker WP (300 MHz) in DMSO-d_6 as the solvent and TMS as an internal reference in Mansoura University. In addition, each metal percentage was determined using a conventional volumetric titration method under the most appropriate conditions as described in the textbook [17]. Also, the qualitative test of chloride content was carried out by using $AgNO_3$ [17] after complete digestion of the complexes using conc. HNO_3. The negative result (no white precipitate) detects there is no presence of chloride with the three complexes completely. This is acceptable especially in presence of NaOAc in the reaction medium and the best ligational ability of acetate group which superior chloride ion.

Quantum aspects

Structural optimization

Gaussian 09 [18] is a well-known molecular dynamics simulation tool that has been approved for structural type validation and is comparable to the single crystal x-ray capability. Becke3-Lee-

Yang-Parr (B3LYP) [18] and valence double zeta polarizing basis set (6-31G*) have indeed been included to the DFT process and adapted to the ligand and its complexes properly. This balanced basis set corresponds to the most well-known split-valence double-zeta plus polarization. This word denotes that the core-orbital is defined by a contract of six Gaussian orbitals, whilst the valence is defined by two. Polarization operations on non-hydrogen atoms are indicated by the star (*). The DFT method was performed at the B3LYP level using integral equation formalism variant (IEF-PCM) and polarizable continuous model to examine ground and excited state properties. The produced computing files (log and chk) were analyzed in Gauss-View and Gauss-Sum 2.2 [19] tools to obtain all quantum properties. The fchk file, on the other hand, was created from the chk file that modified in Gauss-prog panel.

In silico study

A) Pharmacophore search

This simulation strategy aims to evaluate the behavior of new compounds towards COVID-19 depending on the therapeutic history of thiazole-based compounds, recently in COVID-19 treatments. Consequently, the ligand-based discovery model with grid -based model [20] was used to execute pharmacophore quiries (http://pharmit.csb.edu). This *silico* used to look at how thiazole derivative interacts with two COVID-19 proteins (6lu7 and 6lzg) that taken from Protein Database (PDB). Additionally, this study was elongated to handle Paxlovid drug which already now used for treating COVID-19. This drug contains two antivirals as nirmatrelvir and ritonavir that is from thiazole family, for comparison with our compounds. The two proteins chosen for this simulation were 6lu7 and 6lzg as the co-crystals of main protease complex of COVID-19 and the receptor of coronavirus spike, respectively according to PDB. Each PDB file was imported as a source of receptors and then the features were loaded by inserting hydrogen atoms over receptors. After that, each tested compound was loaded as a mol2 file into program screen to start the simulation and obtaining the targeted interaction patterns. Finally, run to search on analogues drugs within MolPort and Zn libraries that updated regularly and aggregating 112,939,594 and 123,399,574 compounds, respectively [21]. Then, we could estimate the number and the types of H-bonding inside the interaction patterns obtained.

B) Molecular operating environmental docking (MOE)

The MOE module (version 2018) was used to capture all interactions features of synthesizes or the approved antivirals (nirmatrelvir and ritonavir) with COVID-19 proteins (6lu7 and 6lzg). Regulation of these proteins, which have a multiplication function in COVID-19 cells [22], is a useful target. Furthermore, one of the two antivirals (ritonavir) is a thiazole derivative, and it has recently been employed in treatment of COVID-19. As a result, this *in-silico* study was designed to compare the antiviral efficiency of the novel thiazole-based compounds with the two drugs and rank their activity. To be appropriate, both of the tested compounds and the COVID-19 proteins should be orientated independently before beginning each docking operation.

The atomic charges and potential energy of each compound were measured after that they were exposed to energy minimization. The consecutive orientation processes were proceeded by creating new database to save the compound as MDB format [23]. Before adding H-atoms, the water must be removed from protein receptors and dummies which adapt to MMFF-force field. After that, attach receptor classes, regulate potential energy, and then run the site-finder to locate allosteric binding receptors or dummies. As a result, after selecting the protein helix, the docking operation on the saved MDB-file can begin. The approach progresses from 30 poses explored to the proper docking pose [24]. Some poses were rejected because of the unfavorable collisions between protein pockets and inhibitors. The qualified hit score and the H-bonding time, which

must be ≤ 3.5 Å, were used to determine the interacting capability of all chemicals examined. The energy score values were calculated using known formula [25]. Additionally, the docking structures as well as the interaction parameters were assessed to identify the inhibitory activity against coronavirus.

Cytotoxicity by MTT method

At the Research Centre, the toxicity of the complexes was tested against tumor cell lines, including liver carcinoma (HepG2), prostate cancer (PC3), and breast cancer (MCF-7) using 4,5-methyl-2-thiazolyl)-2,5-diphenyl-2*H*-tetrazolium bromid MTT assay [26, 27]. The toxicity of 5-fluorouracil (5-Fu), as a common anticancer medication, was measured in terms of 50% inhibition of cell viability (IC_{50} values). On the basis of the mentioned study [27], the synthesized materials were submitted to MTT viability assay. This practical method relies on mitochondrial reductase activity inside living cells to convert yellow 3-(4,5-methyl-2-thiazolyl)-2,5-diphenyl-2*H*-tetrazolium bromide into purple formazan product. The cells were grown in RPMI 1640 medium that completed with 10% fetal bovine serum for assay. 96-well culture plates were loaded with cells immersed in media (2×10^4 cells/mL) and incubated for 12 hr at 37 °C in 5% CO_2 incubator. The tested sample (2 µL) was mixed with 2×10^4 cells in 96-well plates and grown for 3 days at 37 °C. The cultivated cells were combined with 20 µL of MTT solution and placed at 37 °C for 4 h. After removing the supernatant from each well, the formazan crystals were decomposed after adding 100 µL of DMSO to each well to generate the cellular reduction of MTT. The absorbance of each well was evaluated using a microplate reader at λ_{max} = 570 nm after mixing with a mechanical plate mixer. The data were recorded as IC_{50} values, which indicate that the treating cells' proliferation is inhibited by 50% when compared to control cells' development.

RESULTS AND DISCUSSION

Analytical data

The molar ratio inside the complexes was 1:1 (M:L) depending on the analytical results (Table 1). The complexes are stable during storing in desiccators and insoluble in common solvents while are completely soluble in DMSO. The conductivity of 1 mmol in DMSO was measured for the three complexes and the values point to their electrolytic nature (Table 1). The measured values (Λ_m) were from 33.7 to 42.1 $\Omega^{-1}cm^2mol^{-1}$ range, detecting the mono-anionic property of the complexes [28]. As we told previously (synthesis section) the chloride did not found in the complexes completely. This indicates that the electrolytic nature may be due to acetate anion which found in the reaction medium.

Synthesis of thiazole-based ligand (CET)

The key of our research paper, 2-amino-5-(4-ethoxycarbonyl-phenylazo) thiazole **(3)** was prepared by the electrophilic diazo-coupling reaction of 2-aminothiazole **(1)** and the diazotized ethyl 4-aminobenzoate (Scheme 1). Diazotization of ethyl 4-aminobenzoate (2) has been achieved by treatment with sodium nitrite and conc. HCl at 0-5 °C. The obtained diazonium chloride was coupled with 2-aminothiazole in ethyl alcohol and sodium acetate at the most reactive site of thiazole, the fifth position (C-5) rather than the fourth one (C-4). The IR spectrum of compound **3** revealed absorption bands at 3341; 3337 and 1693 cm^{-1} corresponding to amino (NH_2) and carbonyl (C=O) groups, respectively. Its ^1H NMR spectrum exhibited signals at 1.32 ppm (triplet) and 4.31 ppm (quartet) for the ethoxy group of ester ($-OCH_2CH_3$). The aromatic protons resonated as two doublet signals at 7.70 and 8.01 ppm while the singlet signal at 8.15 ppm indicated the

proton of thiazole-C_4. The singlet signal at 8.61 ppm (exchangeable after addition of D_2O) indicated the protons of amino group (NH_2).

Chloroacetylation of 2-aminothiazole derivative **3** was achieved by stirring with chloroacetyl chloride in dry dimethylformamide and anhydrous K_2CO_3 to afford 2-chloroacetamido-5-(ethoxycarbonyl-phenylazo) thiazole **(4)**. The structure of compound **4** was confirmed by spectroscopic techniques including IR and ^{1}H NMR. Its IR spectrum exhibited absorption bands at 3160, 1723 and 1688 cm^{-1} corresponding to the NH, carbonyl-ester (COOEt) and carbonyl amide ($NCOCH_3$) groups, respectively. Its ^{1}H NMR spectrum revealed triplet and quartet signals at 1.34 and 4.35 ppm for the ethoxy group ($-OCH_2CH_3$), singlet at 4.48 ppm for two protons ($NCOCH_2Cl$). The aromatic protons resonated as two doublet signals at 7.84 and 8.08 ppm while the singlet signal at 8.53 ppm indicated the proton of thiazole-C_4. The singlet signal at 12.99 ppm (exchangeable by addition of D_2O) for one proton of chloroacetamide moiety ($NHCOCH_2Cl$).

Table 1. Analytical and physical data of thiazole-based ligand (CET) and its complexes.

Compound empirical formula F.W. found (calculated)	Color	MP (°C)	Yield (%)	%Found (Calcd.)					
				C	H	Cl	N	M	Λ_m*
1) CET; $C_{14}H_{13}ClN_4O_3S$ (352.80)	Orange	220-222	59	47.85 (47.66)	3.77 (3.71)	10.10 (10.05)	15.79 (15.88)	--	-
2)[Co(OAc)(CET)](OAc); $C_{18}H_{19}ClCoN_4O_7S$ (532.21; 529.82)	Greenish brown	> 300	75	39.11 (40.81)	3.79 (3.61)	6.72 (6.69)	10.34 (10.57)	11.15 (11.12)	35.9
3)[Ni(OAc)(CET)](OAc).2H_2O; $C_{18}H_{23}ClN_4NiO_9S$ (532.35; 565.61)	Faint brown	> 300	80	38.61 (38.22)	3.88 (4.10)	6.33 (6.27)	9.47 (9.91)	10.41 (10.38)	42.1
4)[Cu(OAc)(CET)(H_2O)$_2$](OAc).2H_2O ;$C_{18}H_{27}ClCuN_4O_{11}S$ (606.49)	Brown	> 300	83	35.40 (35.65)	4.27 (4.49)	5.90 (5.85)	9.01 (9.24)	10.24 (10.48)	33.7

* in DMSO ($ohm^{-1}cm^2\ mol^{-1}$).

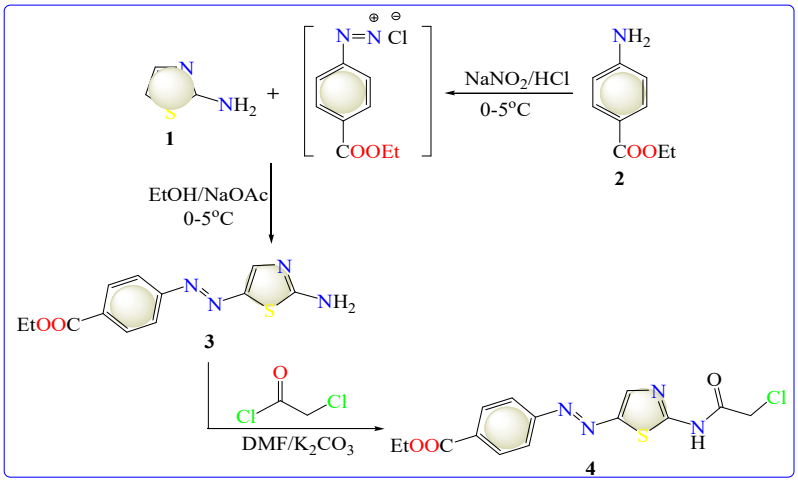

Scheme 1. Synthesis of 2-chloroacetamido-5-(ethoxycarbonyl-phenylazo) thiazole (CET) ligand.

IR and ^{1}H NMR spectroscopy

The new thiazole-based ligand (CET) was coordinated with Co(II), Ni(II) and Cu(II) ions to yield three corresponding complexes. These complexes were basically scanned by IR-spectroscopy, to investigate the shifts recorded to the functional groups. This information could being obtained *via*

comparing the spectrum of the ligand with its complexes, to estimate the affected functional groups. The ligand behaved as a neutral bidentate during the coordination with the metal ions used. This proposal was confirmed firstly by the significant shift of $\nu(C=O)_{amide}$ and $\nu(C=N)$ groups from 1688 and 1600 cm^{-1}, respectively, in the three complexes. On the other side, the vibration of NH was shifted to higher wavenumber, referring to its ruling out from the coordination [29]. The crystal water molecules that suggested with [Ni(OAc)(CET)](OAc).$2H_2O$ and [Cu(OAc) (CET)$(H_2O)_2$](OAc).$2H_2O$ complexes, lead to broadness noticed around 3400 cm^{-1}. This suggestion will be confirmed later through thermogravimetric analysis (TGA). Regarding the complexes spectra, new bands were observed at ≈ 1480 and 1440 cm^{-1} which attributed to ν_{as}(OAc) and ν_s(OAc) vibrations respectively [30]. The difference between the two bands (< 100 cm^{-1}) signifies the bidentate binding of the group. While, the ionic acetate group was confirmed *via* the molar conductivity values that reported in the previous section. Further, the metal-ligand bonds were recorded at ≈ 600 and ≈ 520 cm^{-1}, detecting the vibrations of ν(M-O) and ν(M-N) bands, which agree with the mode of bonding suggested. Moreover, the ^{1}H NMR spectrum of Ni-complex displayed the characteristic signal of acetate group as indicated by the protons of methyl group (singlet at 2.21 ppm). In addition to other expected signals of ethyl, methylene, aromatic and NH protons. ^{1}H NMR (DMSO-d_6): δ_{ppm} 1.21 (t, J = 7.00 Hz, 3H, $OCH_2\underline{CH_3}$),), 2.21 (s, 2H, $COCH_3$), 4.12 (q, J = 7.00 Hz, 2H, $O\underline{CH_2}CH_3$), 4.32 (s, 2H, $COCH_2Cl$), 7.65 (d, J = 8.40 Hz, 2H, Ar-H), 8.05 (d, J = 8.40 Hz, 2H, Ar-H), 8.50 (s, 1H, thiazole-H_4), 12.00 (s, 1H, CONH).

Electronic spectra and magnetism

To promote transition of electrons inside the chemical compounds, you must scanned the samples under UV-Vis radiation either in its dissolved form (in DMSO) or in its solid form (nujol mull). Here, we scanned the dissolved samples of the complexes, after detecting the negligible role of the solvent on the complexes due to no noticeable change in their colors after dissolving. The scan was carried out over 200-1000 nm range, to facilitate all transitions belong intraligand, charge transfer (CT) and d-d transitions (ligand field) within the complexes (Figure 1) [31]. The spectrum of [Co(OAc)(CET)] (OAc) complex showed transitions at 27,778 (360 nm) and 22,272 cm^{-1} (449 nm) which assigned to CT. While, the transition at 16393 cm^{-1} (610 nm) assigns to $^4A_2(F)\rightarrow{}^4T_1(F)$(ν_3) transition that belongs to ligand field (LF) [31]. This LF transition attributes to the tetrahedral geometry around the Co(II) ion. Additionally, the parameters belong to LF as Racah parameter (B), nephelauetic ratio (β) and the LF stabilization energy (Δ = 10 Dq) were calculated. Such calculations depend on LF band as well as the magnetic moment estimated ($\mu_{eff.}$ = 4. 62 BM) by the magnetic susceptibility balance *via* known equations. The value of B was changed from that of free Co(II) ion (971 cm^{-1}) to that of the new Co(II)-Ligand bonds, and the value of β matches the new Co(II)-Ligand bonds' ionic characteristic. Due to orbital-orbital contribution, the magnetic moment for high spin tetrahedral Co(II) complex is larger than the spin only moment value (4.43 BM).

The spectrum of [Ni(OAc)(CET)](OAc).$2H_2O$ complex showed transitions at 26,954 cm^{-1} which assigned to CT for Ni-O or Ni-N type [32]. While, the band appeared at 18,530 cm^{-1} assigned to LF transition of $^1A_1g\rightarrow{}^1B_1g$ type inside the square-planer geometry centered by Ni(II) ion. The diamagnetic property appeared (μ_{eff} = 0) reflects the paring of electrons in d^8 system during formation of dsp^2 hybridization [33]. The [Cu(OAc)(CET)$(H_2O)_2$](OAc).$2H_2O$ complex showed a magnetic moment value (1.70 BM), which is comparable to that of d^9-systems. In addition, its UV-Vis spectrum (Figure 1) reveals a band at 26,525 cm^{-1} (377 nm) that is assigned to CT in a tetragonally distorted octahedral structure. The LF transitions, on the other hand, were seen at 20,964 cm^{-1} (477 nm) and 14824 cm^{-1} (broad band at 675 nm), which could being to $^2B_{1g}\rightarrow{}^2E_g$ and $^2E_g\rightarrow{}^2A_{1g}$ transitions, respectively [34, 35]. Finally, Scheme 2 displayed the suggested structures of the three complexes.

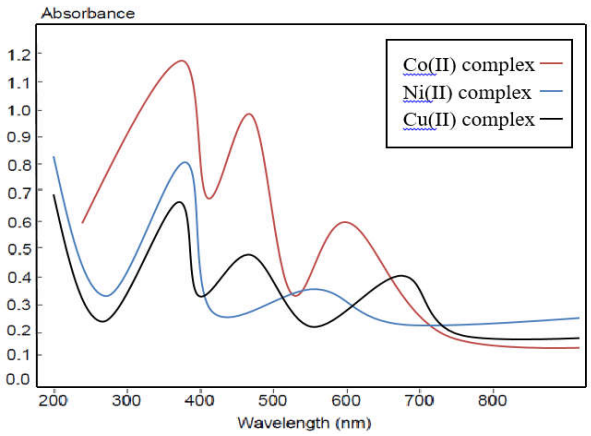

Figure 1. UV-Vis spectra of the studied complexes in DMSO solvent.

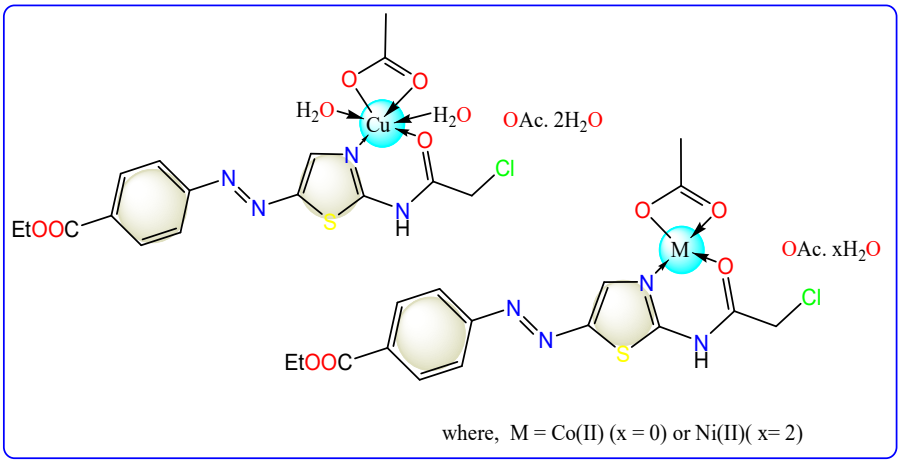

Scheme 2. The structural forms of new thiazole-based complexes.

TGA and kinetics

This analysis was performed for Ni(II) and Cu(II) complexes to assess presence of water molecules that suggested to be found with these complexes based on elemental and IR analyses. The degradation curves were performed at a fixed rate of heating (10 ºC min^{-1}) and over the range of 20-800 ºC. Also, the plausible thermal degradation of the two complexes were tabulated. The curves of the two complexes exhibited four degradation steps starting from ≈ 31 ºC, which detects the thermal instability of the two complexes. The first step showed the expel of the crystal water molecules in the two complexes in addition to the coordinating molecules in the Cu(II) complex. The successive three steps showed a complete distortion for the structural building of the complexes until ≈ 790 ºC. At this point, we recorded the residual parts which agree with NiO and CuO+6C in the two complexes, respectively.

The parameters of the kinetic or thermodynamic estimated from thermal decomposition of Ni(II) and Cu(II) complexes were calculated by utilizing known equations. The relations were drawn according to Coats–Redfern and Horowitz–Metzger equations. Then the values of parameters were calculated for the first three degradation steps in the two curves and tabulated. Consequently from the data displayed we could conclude the following information; 1- For all decomposition stages of complexes, first-order rate was the best fit in every case. 2- The activation enthalpy for the first degradation was determined to be lower because of ejection for water molecules that occurs comparatively fast. 3-When negative activation entropy (ΔS) is found, complexes are more stimulated than reactants [29]. 4- The positive value of ΔH denotes the endothermic character of decomposition processes. 5- The reduction in the decomposition rate from one stage to another was shown via increasing the ΔG value. 6-Furthermore, the positive sign of ΔG detects that the ultimate residual quantity was bigger than the starting stage, indicating a non-spontaneous decomposition process.

Mass spectroscopy

This analytical framework adds further supporting for the molecular formula proposed for two new complexes (Co(II) and Ni(II)), especially with the inability to separate or studying single crystals. This scanning was carried out at a heating rate of m/z = 50-1000 and a temperature of less than 40 °C/min at 70 eV. After evaporating the sample, a beam of electrons was used for collision-induced ionization, which leads to produced molecular ion that effectively fractionated into smaller masses. The mass/charge values of these particles were registered in the patterns exhibited, and they were sorted accordingly. The molecular ion peak of Co(II)-CET complex was appeared at m/z = 532.21 (calcd. 529.82; I = 10), which fits exactly to $[M^{+}+2]$ ion. This difference in mass value is owing to isotopes of chloride which may be found. When this ion is exposed to accelerated electrons, it produces a series of fragmentation peaks (Figure 2), including the base peak (m/z = 377.69; I = 100%), which corresponds to $[C_{14}H_{13}N_4O_3S]^{+}$ moiety. Furthermore, cobalt isotopes produce peaks below to m/z = 65.

In addition, the spectrum of Ni(II)-CET complex exhibited the molecular ion peak at m/z = 532.35 (I = 8, calcd. 565.61), which could be related to $([M^{+}+2]-2H_2O)$ ion. The observed difference between the found and calculated mass due to expel of crystal water molecules during the vaporization process prior the bombardment of electrons [36]. Lastly, it's worth noting that the base peak recorded at m/z = 56.98 corresponds to the metal isotope that was primarily visible during the complex's fragmentation.

EDX and XRD studies

Energy-dispersive X-ray microanalysis (EDX) has being used to confirm the production of selected complexes (i.e. Figures 3) as well as to assess the quantity of elements in the compound (wt %) [37]. The solid specimens (complexes) were placed to a beam of accelerated X-ray photons. The intense photons could enter the inner shells (K- or L-shell) and interact directly with core-electrons. These electrons were easily dragged from their ground orbitals and stimulated to higher levels, leaving positive holes that could be filled with electrons from upper shells such as the L- or M-shell. During relaxation the lost photons able to draw K- (Ka1, Ka2, or Kb) or L-series. The L-series was crucial in this assessment since it allowed us to assess the percentage of each element. As we all know, each element has its own electronic configuration, which corresponds to the development of a singlet-set of peaks that is characteristic for such element. In addition, the heavier element (metal and Cl) was utilized as the basic marker for all percentages (wt%), while the lighter elements (C, H, and O) were omitted. The validation was carried out over a long period of time at several sites in order to obtain better signals. The computed elemental molar ratios (wt/At %) appeared to be close to those derived from elemental analysis.

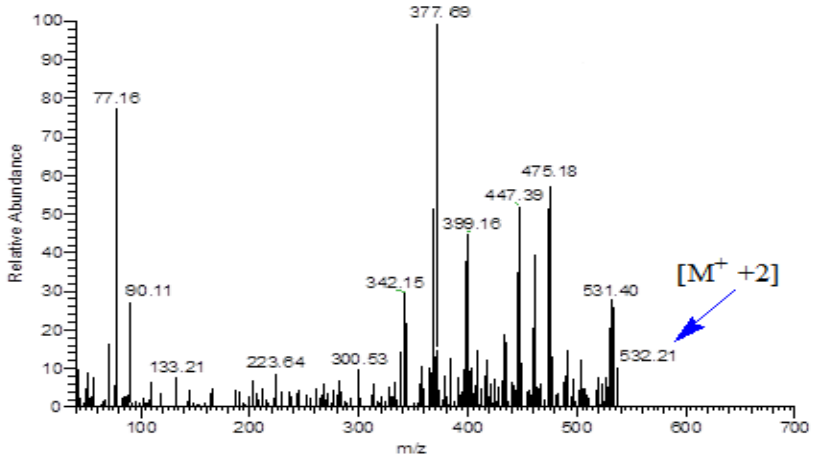

Figure 2. The mass spectrum of Co(II)-CET complex

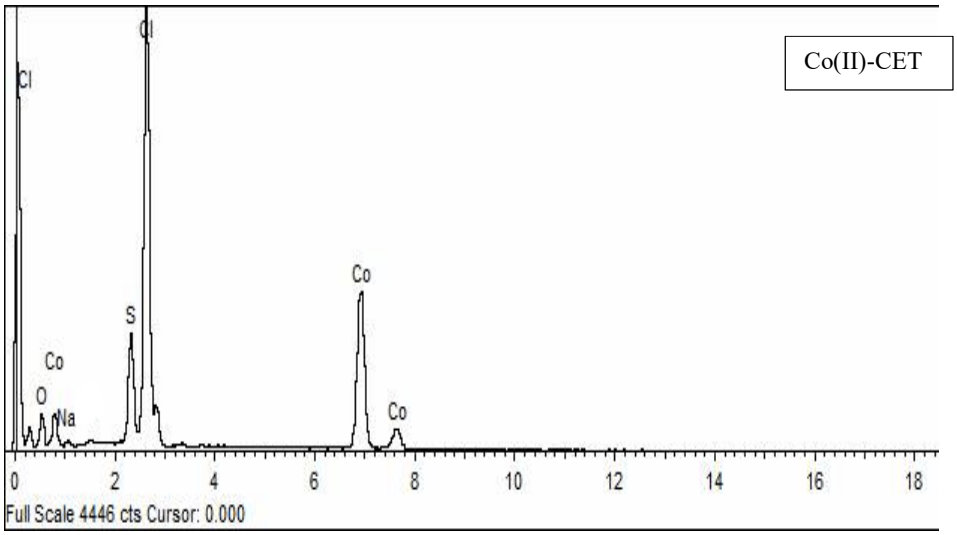

Figure 3. EDX scan for Co(II)-CET complex

The X-ray diffraction methodology (XRD) is useful for determining the degree of crystallinity in solid substances. The patterns were produced throughout the range of $10^{o} < 2\theta < 80^{o}$ (Figures 4) [38]. The X-ray beam was generated from Cu/K_{α} source. Sharp peaks could be seen in the patterns, indicating that these compounds have well–defined crystalline particles. Therefore, the crystal parameters were determined using FWHM approach, including the crystallite size from the Deby–Scherrer equation [$\beta = 0.94\ \lambda/(S \cos \theta)$]. Where B: is the line thickness at half maximum height, θ: is the intense peak diffraction angle, S: is the crystallite size, and Cu/Kα (λ) = 1.5406 Å

[39]. The d-spacing between the interior layers, on the other hand, was calculated using Bragg equation ($n\lambda = 2d\sin(\theta)$, at n = 1). The lattice constants 2θ°, d (Å), FWHM (β), I, and the size S (nm) calculated for the complexes were 15.846°, 5.58829, 0.4667, 5.97, and 31.316 for the Co(II)-CET complex, and 47.053°, 1.92973, 0.0675, 35.2 and 23.39 for the Ni(II)-CET complex, respectively. Further, the Cu(II)-CET complex's lattice constants were 32.301°, 2.76922, 1.1115, 8.21, and 13.577. For the examined compounds, the sizes detect perfect crystalline nano-particles, which is a potential attribute in a variety of applications.

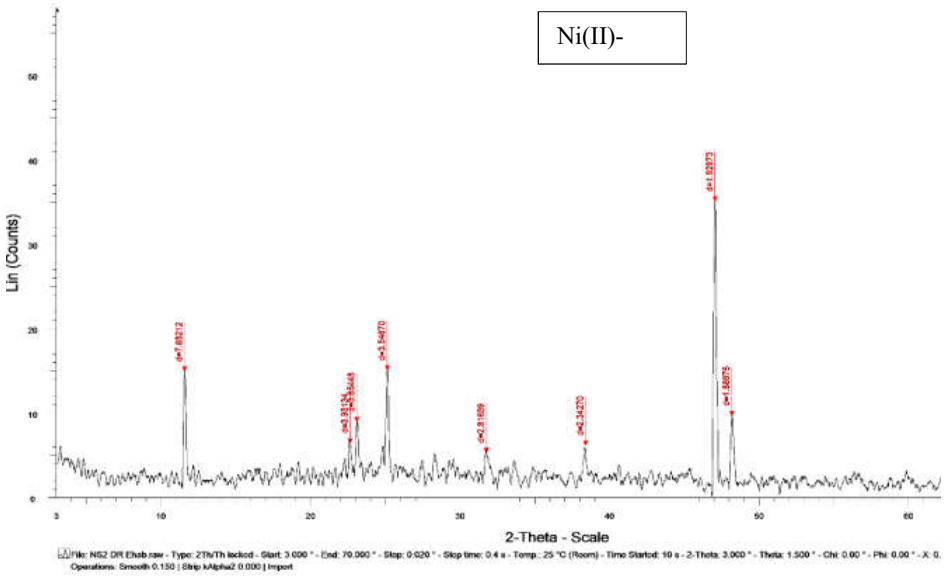

Figure 4. XRD pattern of Ni(II)-CET complex.

Quantum aspects

Structural optimization

The quantum calculations take importance in the last decades and caused revolutionary in the scientific researches based on high credibility of equations used. Gaussian 09 program achieved such importance particularly with unavailability of X-ray single crystallography in our labs. All structures were optimized under 6-31G* basis set and the exported files were visualized based on standard scheme of numbering to extract parameters (Tables 2) and maps (Figures 5) for investigation and analysis.

A) Common features

The structures of CET ligand and its complexes were cleared to recognize the orientation of the functional groups before and after the complexation. The appearance of C(7)=O(13) and C(1)=N(2) groups is favorable for their coordination with the metal ions. Although, the cis-orientation of N(6) and S(5) atoms but they did not contribute in the coordination with the metal ions. This suggestion was supported by Mullikan's charges on the donor atoms. The high

negativity of O13 and N2 atoms is helpful for their coordination perfectly. While, the positivity of N6 and S5 prevents their coordination due to high electrophilic property [40, 41]. The charges of O13 and N2 atoms are significantly reduced in the Co(II)-CET and Ni(II)-CET complexes. Whereas, their charges were elevated in the Cu-CET complex due to metal-ligand CT which is known for the Cu(II) complexes through π-back donation [41]. Also, the charges of the metal ions were efficiently shifted from the starting charge (+2) which considered as a legal feature after coordination.

The bond lengths (Å) for some functional groups within the structures of the ligand and its corresponding complexes, were determined and tabulated (Table 2). The lengths of C(7)=O(13), C(1)=N(2), N(10)-N(11) and C(19)=O(20) were estimated to monitor their changes after complexation. The lengths of C(7)=O(13) and C(1)=N(2) groups suffer elongation inside the complexes while the N(10)-N(11) and C(19)=O(20) groups were more or less unaffected. On the other hand, some bond angles were determined and also displayed to evaluate the degree of uniformity of the new structures. The bond angles within the ligand structure as O(13)-C(7)-N(6), N(6)-C(1)-N(2), C(4)-N(10)-N(11) and O(20)-C(19)-O(21) are coinciding with sp^2 hyberdization of carbon atoms. In the complexes, the angles of O(13)-C(7)-N(6) and N(6)-C(1)-N(2) are relatively shifted from the normal value (120°). Additionally, the bond angles centered by the metal ions appeared close to the values of the suggested geometries as, a tetrahedral of Co(II)-CET, square planer of Ni(II)-CET and octahedral of Cu(II)-CET complex. While, the slight shifts in their values indicates a degree of structural distortion which may refer to different coordinating atoms (NO) and Jahn Teller effect that appeared in Cu(II)-CET complex [42, 43].

Table 2. Significant parameters estimated from molecular modeling of the compounds

The compound	Bond Lengths (Å)		Bond angles (°)	
CET	C(7)=O(13)	1.20861	O(13)-C(7)-N(6)	122.64
Dipole moment = 6.7276 Debye	C(1)=N(2)	1.31395	N(6)-C(1)-N(2)	126.50
Formation energy = -1843.95 a.u.	N(10)-N(11)	1.26855	C(4)-N(10)-N(11)	114.72
	C(19)=O(20)	1.22842	O(20)-C(19)-O(21)	120.27
Co(II)-CET	C(7)=O(13)	1.20874	O(13)-C(7)-N(6)	122.65
Dipole moment = 6.6975 Debye	C(1)=N(2)	1.31451	N(6)-C(1)-N(2)	126.45
Formation energy = -3456.45 a.u.	N(10)-N(11)	1.26969	O(40)-Co(37)-O(41)	101.58
	C(19)=O(20)	1.22832	O(13)-Co(37)-N(2)	107.99
Ni(II)-CET	C(7)=O(13)	1.20863	O(13)-C(7)-N(6)	122.65
Dipole moment =7.1766Debye	C(1)=N(2)	1.31459	N(6)-C(1)-N(2)	126.45
Formation energy = -3581.58 a.u.	N(10)-N(11)	1.26962	O(40)-Ni(37)-O(41)	87.58
	C(19)=O(20)	1.22836	O(13)-Ni(37)-N(2)	82.10
Cu(II)-CET	C(7)=O(13)	1.22374	O(13)-C(7)-N(6)	141.79
Dipole moment = 4.6064 Debye	C(1)=N(2)	1.31451	N(6)-C(1)-N(2)	126.14
Formation energy = -3862.89 a.u.	N(10)-N(11)	1.26893	O(47)-Cu(37)-O(50)	89.69
	C(19)=O(20)	1.22826	O(42)-Cu(37)-O(40)	80.12

B) Global reactivity

To predict the bioavailability of the studied substances, relevant indices were determined using conventional formulae [44] depending on E_{LUMO} and E_{HOMO} values. The indicators that calculated were absolute-softness (σ), global softness (S), global hardness (η), chemical potential (μ), electrophilicity (ω), and electronegativity (χ). We can draw the following conclusions based on the projected values: (i) if the complexes' softness property exceeds than that of their ligand, we can expect their superiority in biomedical field. (ii) The electrophilicity scores of the complexes are likewise higher than those of the ligand, indicating that these compounds have a great propensity to take electrons from their surroundings. (iii) Furthermore, the complexes' high energy gabs (ΔE) represent their tolerance towards electronic transitions. Table 2 shows that the dipole

moment (Debye) values are less; this could be attributed to decreased polarity over the molecules, which is preferable in biological efficiency. The formation energy values (a.u.) show that the produced complexes are quite stable [44].

C) 3-D maps

Over cubic surfaces of the compounds, the HOMO and LUMO levels were created (Figure 5). The following were the characteristics of the two frontier orbitals; regarding the ligand, the functional groups which included the donor atoms, were well covered by the two frontier orbitals. This shows how adaptable their electronic-clouds during the coordination. The complexes imaging, on the other hand, showed the two levels focused on the core metal atoms and their environment [42].

The location of electronic cloud on the functional groups was also differentiated using electrostatic potential maps. By differentiating nucleophilic, electrophilic, and neutral zones in the ligand, this map can be utilized to investigate the nucleophilicity of groups towards the metal ions then analyzing the binding mechanism. The colors red, blue, and green were used to depict these three parts. The electrostatic potential of the free ligand showed brightly the nucleophilic and electrophilic zones. The nucleophilicity of O(13) and N(2) atoms was clearly visible, showing their capacity to coordinate with metal ions. While, the electrophilicity of N(6) and S(5) was clearly noticed, indicating their inability to coordinate with the metal ions. Regarding the maps of the three complexes, the nucleophilicity of O(13) and N(2) atoms was notably reduced. Whereas, the overall nucleophilicity in the complexes was improved due to the coordination of acetate or water molecules as a secondary ligands [43, 44].

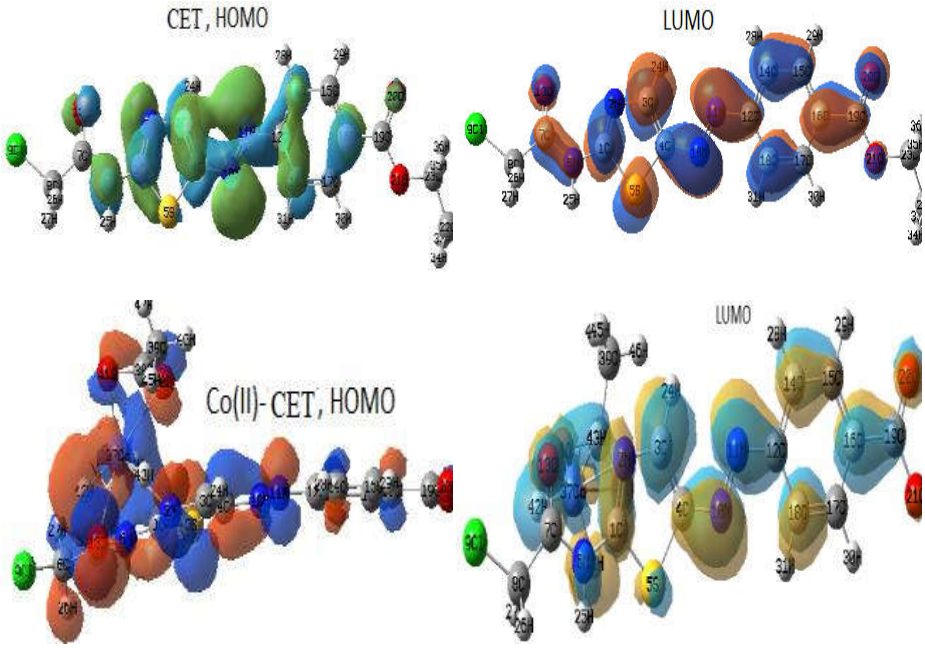

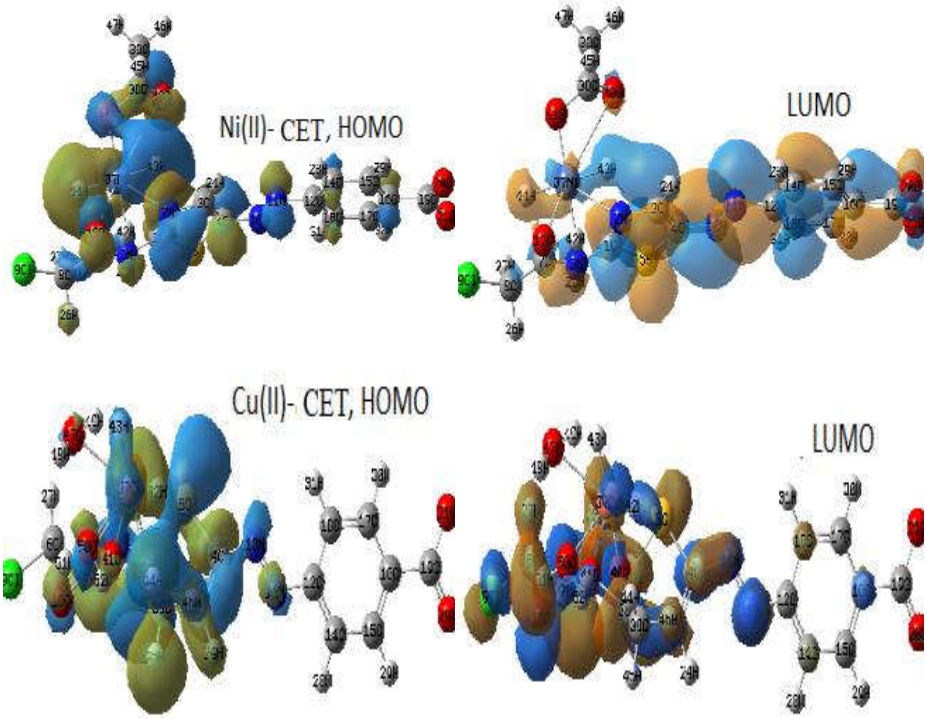

Figure 5. 3D images of two frontier orbitals for thiazole-based ligand and its new complexes.

In-silico assessments versus COVID-19

This simulation aims to evaluate the behavior of CET ligand and its complexes versus COVID-19 depending on the therapeutic history of thiazole-based compounds, recently in COVID-19 treatments. The goal of this research is to look at how thiazole derivative interacts with two COVID-19 proteins (6lu7 and 6lzg). Also, we oriented our study for comparison with Paxlovid drug which contains two antivirals (nirmatrelvir and ritonavir) and recently used for treating COVID-19. The ritonavir drug is a thiazole-based compound as our ligand which may success also in coronavirus treatment or one of its complexes. The two proteins chosen for this simulation were 6lu7 and 6lzg as the co-crystal structures of main protease complex of COVID-19 and the receptor of coronavirus spike, respectively. This selection is based on their role in cell growth of virus and their inhibition is a perfect target.

A) Pharmit profile

An introductory view about the therapeutic activity versus targeted proteins could being built through this *in-silico* way [53, 54]. Consequently, we aimed to investigate the new thiazole-based ligand (CET) and its complexes versus receptors of COVID-19 (6lu7 and 6lzg) compared to selected antivirals (nirmatrelvir and ritonavir). The interaction patterns for all processes were yielded (Figures 6), for investigation. The magnitude of interaction for all compounds as well as the two antivirus with 6lu7 protein is lesser than their interactions with 6lzg protein which is highly

effective. The best interaction was observed from ritonavir drug and the Co(II)-CET complex with the two proteins especially with 6lzg one. The interaction of the free CET ligand in very poor compared to its complexes. The inhibition activity of Co(II)-CET complex exceeds than the nirmatrelvir drug. So, this complex may be used instead of it in Paxlovid drug to increase its efficiency towards COVID-19 virus, which still irritating the world. This inhibition activity recorded from Co(II)-CET complex which exceeds than the free ligand, may refer to the cobalt ion inserted in the organic compound. As known, the cobalt ion could bind to the hydrophobic pockets inside the enzymes and its complexes played as antivirals perfectly [47]. The types of H-bonding formed inside the interaction patterns of Co(II)-CET, nirmatrelvir and ritonavir with 6lzg protein were H-acceptor (acc) and H-donor (don) (Table 3). On the other hand, a pharmacophore query was run for each new compound inside MolPort and Zn libraries to find any analogues drugs, but we did not reach to anyone.

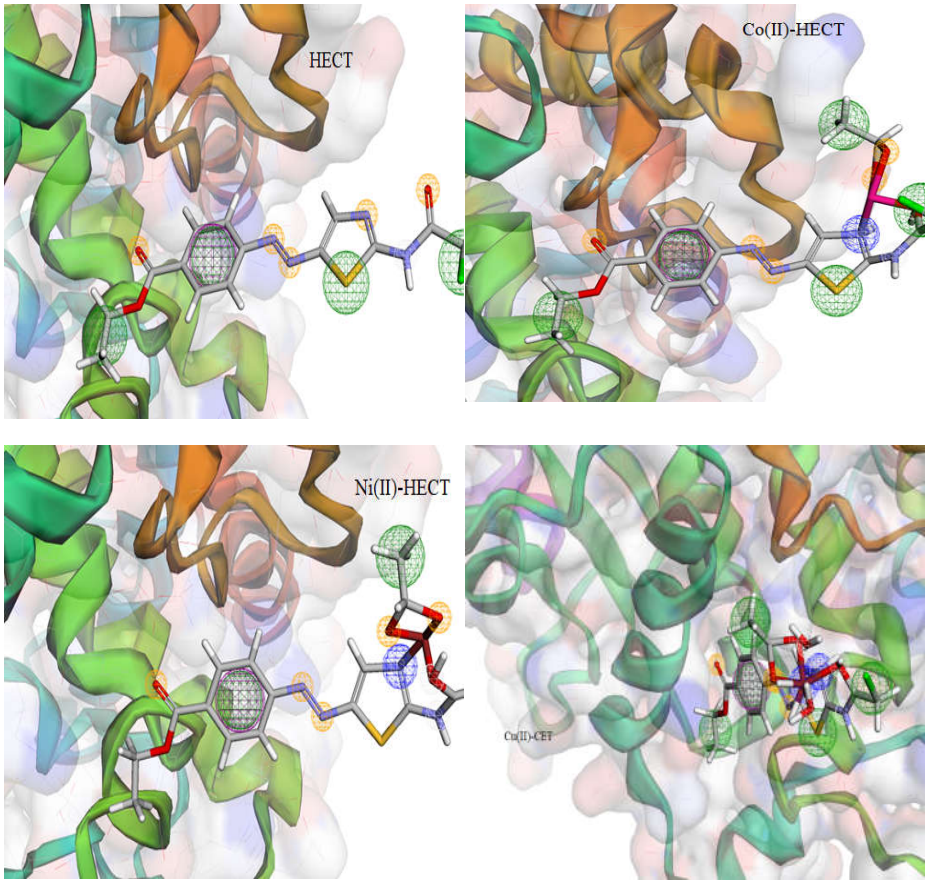

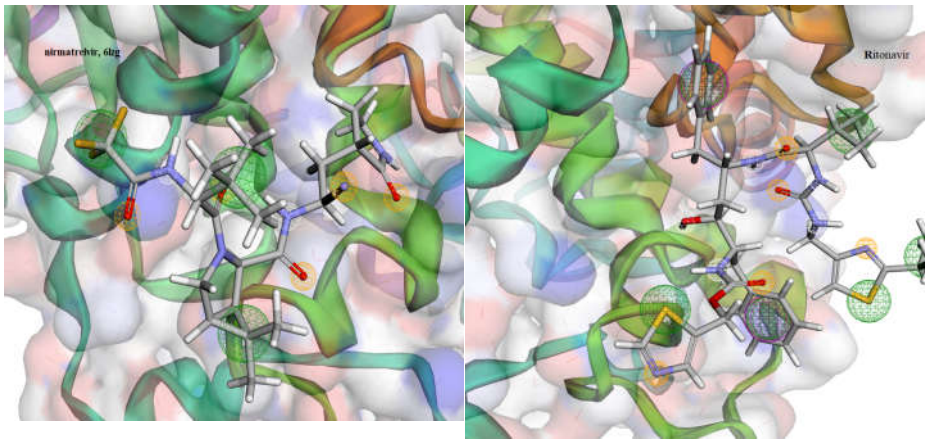

Figure 6. Pharmacophore search for the interaction with 6lzg protein of COVID-19.

B) Molecular operating environmental (MOE) docking

In the previous section (A) we introduced *in-silico* assay of two recommended antivirals in treatment of COVID-19 compared to our new compounds *via* Pharmit link. The outcomes suggest the superiority of ritonavir drug and our new Co(II)-CET complex in the interaction with two COVID-19 receptors. This suggests the successful use of Co(II)-CET complex instead of nirmatrelvir in the Paxlovid drug to treat recent coronavirus. While, the whole interaction features cannot obtained from this *silico* way, while the MOE-docking offers a deep information about the interaction validity [48]. The two antivirals (nirmatrelvir and ritonavir), CET, Co(II)-CET and Ni(II)-CET were the potential inhibitors treated in this simulation against receptors of COVID-19 (6lu7 and 6lzg). The interaction patterns and the docking parameters (Table 3) were obtained and investigated to display the following remarks; (i) The docking score values lead to this inhibition order; ritonavir-6lzg (-9.1276) > ritonavir-6lu7 (-8.3398) > Co(II)-CET-6lzg (-7.7579) > Co(II)-CET-6lu7 (-6.7341) > nirmatrelvir-6lu7 (-7.0578). This detects the high inhibitory effect of ritonavir drug and the Co(II)-CET complex towards the two proteins [49]. All the docking poses are formed from true allosteric bending with protein pockets *via* normal H-bond lengths ≤ 3.5 Å. The scoring values for CET docking are significant but all its interaction features are missing so its inhibition validity cannot verified. (ii) The H-donor type of binding is predominant in addition to the appearance of H-acceptor type in some cases. The acidic residues (blue circle) were the main residues recorded in the docking patterns and bonded *via* side-chain donor type. Whereas the polar residue (pink circle) was slightly appeared and bonded *via* side-chain acceptor type. (iii) The binding sites from new compounds were N2, O14, O22 and O42, the binding sites from ritonavir drug were N9, N40 and N37, while the binding sites from nirmatrelvir drug were O13, N4, O6 and N10. (iv) The residue of amino acids that interacted as a receptor from 6lu7 protein was GLU166 (A) with Co(II)-CET, Ni(II)-CET and nirmatrelvir drug. While, the CYS 145 (A) was also interacted with Co(II)-CET complex and the ritonavir drug interacted with ASN 142(A) and GLN 189 (A) residues. On the other side, the GLU 406 (A) residue was interacted from 6lzg protein with Co(II)-CET and Ni(II)-CET only. Whereas, the residue interacted with ritonavir drug was ASP 206 (A) and the residues interacted with nirmatrelvir drug were HOH 1034 (A), HOH 833 (A), HOH 940 (A) and HOH 1046 (A). The inhibition of Glutathione (GLU) is very essential due to its vital role in the living cells, so its controlling is a good goal. So, the Co(II)-CET complex exhibited interaction with this amino acid which is favored [49]. (v) The ligand exposure surface was

effectively reduced in most complexes, which detects the saturation of binding for all compounds and there is no probability for extra-bonding can be formed. (vi) The formation energy values were notably lowered in Co(II)-CET docking complexes with both 6lu7 and 6lzg proteins. The values reach to -21.5 kcal/mol with 6lu7 and -18.2 kcal/mol with 6lzg. Also, Ni(II)-CET docking complexes were highly stable the formation energy values were -16.4 and -18.5 kcal/mol with 6lu7 and 6lzg proteins, respectively. While, the stability of nirmatrelvir or ritonavir drug with the two proteins are moderate [49]. Finally, we could suggest the Co(II)-CET complex as antiviral towards COVID-19 which close to the activity of ritonavir drug while exceeds the activity of nirmatrelvir drug. This study may be a starting point for specialist to concentrate their clinical investigations on our new complex, which could being promising.

Table 3. The interaction parameters for docking complexes with two COVID-19 proteins.

Compounds	Proteins	Ligand	Receptor	Interaction	Distance (Å)	E(kcal/ mol)	S (energy score)
CET	6lu7	---	---	---	---	---	-6.1522
	6lzg	---	---	---	---	---	-6.3140
Co(II)-CET	6lu7	N2	OE1 GLU 166 (A)	H-donor	2.84	-6.1	-6.7341
H-acc = 5;		O14	OE1 GLU 166 (A)	H-donor	2.70	-21.5	
H-don = 4		O22	SG CYS 145 (A)	H-donor	3.45	-1.0	
	6lzg	N2	OE1 GLU 406 (A)	H-donor	3.33	-6.7	-7.7579
		O14	OE1 GLU 406 (A)	H-donor	3.28	-5.8	
		O14	OE2 GLU 406 (A)	H-donor	2.65	-18.1	
Ni(II)-CET	6lu7	N2	O GLU 166 (A)	H-donor	3.24	-5.4	-6.7324
		O14	O GLU 166 (A)	H-donor	2.77	-16.4	
	6lzg	O14	OE2 GLU 406 (A)	H-donor	2.69	-18.5	-5.9623
		O42	OE2 GLU 406 (A)	H-donor	2.71	-3.6	
Nirmatrelvir	6lu7	O13	N GLU 166 (A)	H-acceptor	2.86	-3.9	-7.0578
H-acc = 5;	6lzg	N4	O HOH 1034 (A)	H-donor	3.35	-1.5	-6.6106
H-don = 3		O6	O HOH 833 (A)	H-acceptor	3.24	-1.1	
		N10	O HOH 940 (A)	H-acceptor	3.24	-2.1	
		O13	O HOH 1046 (A)	H-acceptor	3.14	-2.1	
Ritonavir	6lu7	N9	OD1 ASN 142 (A)	H-donor	2.94	-3.3	-8.3398
H-acc = 6;		N40	OE1 GLN 189 (A)	H-donor	3.30	-0.7	
H-don = 5	6lzg	N37	OD2 ASP 206 (A)	H-donor	3.44	-1.1	-9.1276
		N40	OD2 ASP 206 (A)	H-donor	3.22	-1.2	

Cytotoxicity

Depending on the *in-silico* results which exhibited the desirable inhibition activity of Co(II)-CET complex towards the recent coronavirus, we intended to investigate the cytotoxicity of these new compounds towards tumors that are not less dangerous than the COVID-19. MTT method [26, 27] was applied to estimate the cell viability of liver carcinoma (HepG2), prostate cancer (PC3), and breast cancer (MCF-7) cells after treatment with the new complexes compared to 5-fluorouracil (5-Fu). The IC_{50} (µg/mL) values were calculated (Table 4) and the Co(II)-CET complex showed the excellent cytotoxicity for liver carcinoma (HepG2) and prostate cancer (PC3) cell lines. The value towards HepG2 cells appeared close to reference drug (5-Fu), while exceeds the reference in PC3 cells. Consequently, the promising biological activity of Co(II)-CET complex was confirmed *via silico* towards COVID-19 and *via in-vitro* towards cancer cell lines, particularly the liver and prostate cancers.

It was known that the biological activity of the chemicals is strongly influenced by the structure of such compound. Consequently here, the existence of thiazole rings, N=N, C=O, and NH functional groups, improves the biological performance of the compounds. They have the potential to increase the penetration of substances across cell membranes, allowing for actively

engaging with biological systems while also inhibiting cell development. According to Tweedy's chelation theory, the metal ion has a substantial effect on the degree of inhibition towards microorganisms. According to this idea, the metal charge is minimized due to coordination until it reaches a limit that allows the complex to be lipophilic which is could miscible with cell lipid and then interface with cell systems. On the other side, the inclusion of the complex molecule on the cell wall could impair the cell's capacity to produce protein, which is necessary for respiration, and so the cell's development was slowed [50]. Also, the quantum data that reported in the previous sections supported the activity of such structures based on the estimated global reactivity indices.

Table 4. Cytotoxic activity against three human cancer cell lines.

Compounds	In vitro cytotoxicity IC_{50} (µg/mL)[a]		
	HePG2	PC3	MCF-7
Co(II)-CET	7.77±0.8	6.52±0.5	8.07±0.7
Ni(II)-CET	51.38±2.4	36.81±2.1	33.19±1.9
Cu(II)-CET	30.55±1.8	26.40±1.5	27.25±2.1
5-FU[b]	7.91±0.3	8.22±0.2	5.60±0.2

[a]IC50 (µg/mL): 1–10 (very strong), 11–20 (strong), 21–50 (moderate), 51–100 (weak), and above 100 (non-cytotoxic). [b]5-FU = 5-fluorouracil is the reference drug for anticancer tests.

CONCLUSION

New Co(II), Ni(II) and Cu(II) complexes were prepared from thiazole-based ligand. The ligand coordinated through neutral bidentate towards the metal ions within different geometries. All available analytical and spectral techniques were used to elucidate the formulae of the ligand and its complexes. The DFT/B3LYP method was applied to configure the structures of all compounds and then confirming the coordination features. The global reactivity indices were calculated and indicated the best physical properties of the complexes. *In-silico* assays were performed against COVID-19 receptors. This is based on the recent use of a thiazole-based compound (ritonavir) in coronavirus treatment. This antiviral was mixed with nirmatrelvir drug in COVID-19 protocol. Consequently, this study was conducted to the two antivirals for comparison with the new compounds. The Co(II)-CET complex as well as the ritonavir drug are appeared with excellent inhibition for COVID-19 receptors. Additionally, we performed *in-vitro* test for cytotoxicity against three carcinoma cell lines, liver carcinoma (HepG2), prostate cancer (PC3), and breast cancer (MCF-7). The Co(II)-CET complex showed superiority than the standard drug (5-fluorouracil) towards HepG2 and PC3 cell lines. Finally, controlling COVID-19 or cancer cells is the main target of scientists and the Co(II)-CET complex may be promising drug towards both of cancer cells and COVID-19 virus.

ACKNOWLEDGMENT

The authors would like to thank the Deanship of Scientific Research at Umm Al-Qura University for supporting this work by Grant Code: (22UQU4350527DSR13).

REFERENCES

1. Refat, M.; Sedayo, A.; Sayqal, A.; Alharbi, A.; Katouah, H. Abumelha, H.; Alzahrani, S.; Alkhatib, F.; Althagafi, I.; El-Metwaly, N. Aurintricarboxylic acid and its metal ion complexes in comparative virtual screening versus lopinavir and hydroxychloroquine in fighting COVID-19 pandemic: Synthesis and characterization. *Inorg. Chem. Commun*. **2021**, 126, 108472.
2. Choppin, P.W.; Compans, R.W. Reproduction of paramyxoviruses. *Comprehensive Virology*, Springer: Boston; **1975**; pp. 95-178.

3. Nichol, S.T.; Arikawa, J.; Kawaoka. Y. Emerging viral diseases. *Proc. Natl. Acad. Sci., U.S.A.* **2000**, 97, 12411.
4. Cascella, M.; Rajnik, M.; Cuomo, A.; Dulebohn, S.C.; Di Napoli, R. *Features, Evaluation, and Treatment Coronavirus (COVID-19)*, Stat Pearls Publishing: Stat Pearls (Internet) Online Publishing; **2022**.
5. Blaising, J.; Polyak, S.J.; P´echeur, E.-I. Arbidol as a broad-spectrum antiviral: An update. *Antivir. Res*. **2014**, 107, 84-94.
6. Du, X.X.; Chen, X.P. Favipiravir: pharmacokinetics and concerns about clinical trials for 2019-nCoV infection. *Clin. Pharmacol. Ther*. **2020**, 108, 242-248.
7. Prusoff, W.H. Synthesis and biological activities of iododeoxyuridine, an analog of thymidine, *Biochim. Biophys. Acta* **1959**, 32, 295-296.
8. Sokolova, A.S.; Yarovaya, O.I.; Bormotov, N.I.; Shishkina, L.N.; Salakhutdinova, N.F. Synthesis and antiviral activity of camphor-based 1,3-thiazolidin-4-one and thiazole derivatives as Orthopoxvirus -reproduction inhibitors, *MedChemComm* **2018**, 9, 1746-1753.
9. a) El-Bindary, M.A.; El-Desouky, M.G.; El-Bindary, A.A. Metal–organic frameworks encapsulated with an anticancer compound as drug delivery system: Synthesis, characterization, antioxidant, anticancer, antibacterial, and molecular docking investigation, *Appl. Organomet. Chem*. **2022**, 36, e6660; b) Kiwaan, H.; El-Mowafy, A.S.; El-Bindary, A. Synthesis, spectral characterization, DNA binding, catalytic and in vitro cytotoxicity of some metal complexes. *Mol. Liq.* **2021**, 326 115381.
10. El-Bindary, M.A.; El-Bindary, A.A. Synthesis, characterization, DNA binding, and biological action of dimedone arylhydrazone chelates. *Appl. Organomet. Chem*. **2022**, 36, e6576.
11. Shih, S.-R.; Chu, T.-Y.; Reddy, G.R.; Tseng, S.-N.; Chen, H.-L.; Tang, W.-F.; Wu, M.-S. ; Yeh, J.-Y.; Chao, Y.-S.; Hsu, J.T.; Hsieh, H.-P.; Horng, J.-T. Pyrazole compound BPR1P0034 with potent and selective anti-influenza virus activity. *J. Biomed. Sci.*, **2010**, 17, 1-9.
12. Makarova, N.V.; Boreko, E.I.; Moiseev, I.K.; Pavlova, N.I.; Nikolaeva, S.N.; Zemtsova, M.N.; Vladyko, G.V. Antiviral activity of adamantane-containing heterocycles. *Pharm. Chem. J.* **2002**, 36, 3-6.
13. Colarusso, S.; Attenni, B.; Avolio, S.; Malancona, S.; Harper, S.; Altamura, S.; Koch, U.; Narjes, F. Inhibitors of the hepatitis C virus RNA-dependent RNA polymerase. *Arkivoc* **2006**, 7, 479-495.
14. Yan, S.; Appleby, T.; Larson, G.; Wu, J.Z.; Hamatake, R.; Hong, Z.; Yao, N. Structure based design of a novel thiazolone scaffold as HCV NS5B polymerase allosteric inhibitors. *Bioorg. Med. Chem. Lett.* **2006**, 16, 5888-5891.
15. Lewis, A.; McDonald, M.; Scharbach, S.; Hamaway, S.; Plooster, M.; Peters, K.; Fox, K.M.; Cassimeris, L.; Tanski, J.M.; Tyler, L.A. The chemical biology of Cu(II) complexes with imidazole or thiazole containing ligands: Synthesis, crystal structures and comparative biological activity. *J. Inorg. Biochem*. **2016**, 157, 52-61.
16. Maret, W.; Wedd, A. *Binding, Transport and Storage of Metal Ions in Biological Cells*, Royal Society of Chemistry: London; **2014**
17. Vogel. A.I. *Quantitative Inorganic Analysis*, Longmans: London; **1989**.
18. Frisch, M.; Trucks, G.; Schlegel, H.; Scuseria, G.; Robb, M.; Cheeseman, J.; Scalmani, G.; Barone, V.; Mennucci, B.; Petersson. G. *Gaussian 09, Revision A1*, Gaussian: Wallingford, CT, USA; **2009**.
19. Becke, A.D. Density-functional thermochemistry. III. The role of exact exchange. *J. Chem. Phys*. **1993**, 98, 5648-5652.
20. Lee, C.; Yang, W.; Parr, R.G. Development of the Colle-Salvetti correlation-energy formula into a functional of the electron density. *Phys. Rev. B* **1988**, 37, 785-789.
21. Perdew, J.P.; Wang, Y. Pair-distribution function and its coupling-constant average for the spin-polarized electron gas. *Phys. Rev. B* **1992**, 46, 12947-12954.

22. Dennington, R.; Keith, T.; Millam, J. *GaussView, Version 5*, Semichem Inc.: Shawnee Mission, KS; **2009**.
23. Willey, C.D.; Bonner. J.A. *Interaction of Chemotherapy and Radiation* in *Clinical Radiation Oncology*, 4th ed., W.B. Saunders: Philadelphia, e-publication; **2016**; pp. 63-79.
24. Sunseri, J.; Ryan Koes, D. Pharmit: Interactive exploration of chemical space. *Nucleic Acids Res.* **2016**, 44, W442–W448.
25. Musyoka, T.M.; Kanzi, A.M.; Lobb, K.A.; Bishop, Ö.T. Structure based docking and molecular dynamic studies of plasmodial cysteine proteases against a South African natural compound and its analogs. *Sci. Rep*. **2016**, 6, 1-12.
26. Mosmann. T. Rapid colorimetric assay for cellular growth and survival: Application to proliferation and cytotoxicity assays. *J. Immunol. Methods* **1983**, 65, 55-63.
27. Mohamed, S.M.; Kotb, E.R.; Abd El-Meguid, E.A.; Awad, H.M. Synthesis and solid-state fluorescence of 2-alkylamino-4-aminopyridine-3,5-dicarbonitriles. *Res. Chem. Intermed.* **2017**, 43, 437.
28. Geary, W.J. The use of conductivity measurements in organic solvents for the characterization of coordination compounds. *Coord. Chem. Rev*. **1971**, 7, 81-122.
29. Abu-Dief, A.M.; El-Metwaly, N.M.; Alzahrani, S.O.; Alkhatib, F.; Abualnaja, M.M.; El-Dabea, T.; Abd El Aleem Ali Ali, M. Synthesis and characterization of Fe(III), Pd(II) and Cu(II)-thiazole complexes; DFT, pharmacophore modeling, in-vitro assay and DNA binding studies. *J. Mol. Liq.* **2021**, 326, 115277.
30. Nakamoto, K. *Infrared Spectra of Inorganic, Coordination Compounds*, Wiley Interscience: New York; **1970**; pp. 25, 232.
31. Lever, A.B.P. *Inorganic Electronic Spectroscopy*, 2nd ed., Elsevier: New York; **1984**.
32. Abumelha, H.M.; Al-Fahemi, J.H.; Althagafi, I.; Bayazeed, A.A., Al-Ahmed, Z.A.; Khedr, A.M.; El-Metwaly, N. Deliberate-characterization for Ni(II)-Schiff base complexes: promising in-vitro anticancer feature that matched MOE docking-approach. *J. Inorg. Organomet. Polym.* **2020**, 30, 3277-3293.
33. Al-Hazmi, G.A.A.; Abou-Melha, K.S.; El-Metwaly, N.M.; Althagafi, I; Shaaban, F.; Elghalban, M.G.; El-Gamil, M.M. Spectroscopic and theoretical studies on Cr(III), Mn(II) and Cu(II) complexes of hydrazone derived from picolinic hydrazide and O-vanillin and evaluation of biological potency. *Appl. Organomet. Chem*. **2019**, 34, e5408.
34. Alkhatib, F.; Hameed, A.; Sayqal, A.; Bayazeed, A.A.; Alzahrani, S.; Al-Ahmed, Z.A.; Zaky, R.; El-Metwaly, N.M. Green-synthesis and characterization for new Schiff-base complexes; spectroscopy, conductometry, Hirshfeld properties and biological assay enhanced by in-silico study. *Arab. J. Chem.* **2020**, 13, 6327-6340.
35. Saber, R.W.; Abou-Melha, K.; El-Metwaly, N. Synthesis of new Cr(III) complexes derived from antipyrine-based ligands: Elucidation, conformation, cytotoxicity and genotoxicity via in-vitro and in-silico approaches. *J. Mol. Liq*. **2022**, 359, 119361.
36. Alatawi, N.M.; Alsharief, H.; Alharbi, A.; Alhasani, M.; Attar, R.; E Khalifa, M.; Abu-Dief, A.M.; El-Metwaly, N.M. Simulation for the behavior of new Fe(III) and Cr(III)-thiophenyl complexes towards DNA polymerase: Synthesis, characterization, eukaryotic DNA and Hartree–Fock computation. *Chem. Pap*. **2022**, 76, 3919-3935.
37. Alkhamis, K.; Alsoliemy, A.; Aljohani, M.M.; Alrefaei, A.F.; Abumelha, H.M.; Mahmoud, M.H.; Zaky, R.; El-Metwaly, N.M. Conductometry of nano-sized zinc sulfate; synthesis and characterization of new hydrazone complexes: Conformational and in-vitro assay. *J. Mol. Liq*. **2021**, 340, 117167.
38. Cullity, B.D. *Elements of X –Ray Diffraction*, 2nd ed., Addison–Wesley Publishing Company Inc.: Boston; **1993**.
39. Velumani, S.; Mathew, X.; Sebastian, P.J.; Narayandass, Sa. K.; Mangalaraj, D. Structural and optical properties ofhot wall deposited CdSe thin films. *Solar Energy Mater. Solar Cell*. **2003**, 76, 347-358.

40. Alzahrani, S.; Morad, M.; Bayazeed, A.; Aljohani, M.; Alkhatib, F.; Shah, R.; Katouah, H.; Abumelha, H.M.; Althagafi, I.; Zaky, R.; El-Metwaly. N.M. *J. Mol. Struct.* **2020**, 1218, 128473.
41. Almalki, S.A.; Bawazeer, T.M.; Asghar, B.; Alharbi, A.; Aljohani, M.M.; Khalifa, M.E.; El-Metwaly, N.M. Synthesis and characterization of new thiazole-based Co(II) and Cu(II) complexes; therapeutic function of thiazole towards COVID-19 in comparing to current antivirals in treatment protocol. *J. Mol. Struct*. **2021**, 1244, 130961.
42. Domazetis, G.; James, B.D. Molecular models of brown coal containing inorganic species. *Org. Geochem*. **2006**, 37, 244-259.
43. Chikate, R.C.; Padhye, S.B. Transition metal quinone–thiosemicarbazone complexes 2: Magnetism, ESR and redox behavior of iron(II), iron(III), cobalt(II) and copper(II) complexes of 2-thiosemicarbazido-1,4-naphthoquinone. *Polyhedron* **2005**, 24, 1689.
44. Al-Hazmi, G.A.A.; Abou-Melha, K.S.; El-Metwaly, N.M.; Althagafi, I.; Shaaban, F.; Zaki, R. Green synthesis approach for Fe(III), Cu(II), Zn(II) and Ni(II)-Schiff base complexes, spectral, conformational, MOE-docking and biological studies. *Appl. Organomet. Chem*. **2020**, 34, e5403.
45. Mu, P.; Karuppasamy, R. Discovery of human autophagy initiation kinase ULK1 inhibitors by multi-directional in silico screening strategies. *J. Recept. Signal Transduct*. **2019**, 39, 122-133.
46. Kandakatla, N. Ramakrishnan, G. Ligand based pharmacophore modeling and virtual screening studies to design novel HDAC2 inhibitors. *Adv. Bioinform*. **2014**, 2014, 812148.
47. Chang, E.L.; Simmers, C.; Knight, D.A. Cobalt complexes as antiviral and antibacterial agents. *Pharmaceuticals (Basel)* **2010**, 3, 1711-1728.
48. Obrecht, A.S.; Urban, N.; Schaefer, M.; Röse, A.; Kless, A.; Meents, J.E.; Lampert, A.; Abdelrahman, A.; Müller, C.E.; Schmalzing, G.; Hausmann, R. Identification of aurintricarboxylic acid as a potent allosteric antagonist of P2X1 and P2X3 receptors. *Neuropharmacology* **2019**, 158, 107749.
49. Angelusiu, M.V.; Barbuceanu, S.F.; Draghici, C.; Almajan, G.L. New Cu(II), Co(II), Ni(II) complexes with aroyl-hydrazone based ligand. Synthesis, spectroscopic characterization and in vitro antibacterial evaluation. *Eur. J. Med. Chem*. **2010**, 45, 2055-2062.
50. Refat, M.; Sedayo, A.A.; Sayqal, A.; Alharbi, A.; Katouah, H.A.; Abumelha, H.M.; Alzahrani, S.; Alkhatib, F.; Althagafi, I.; El-Metwaly, N. Aurintricarboxylic acid and its metal ion complexes in comparative virtual screening versus lopinavir and hydroxychloroquine in fighting COVID-19 pandemic: Synthesis and characterization. *Inorg. Chem. Commun*. **2021**, 126, 108472.